

CHAPTER 6: Modeling the Active Membrane Surface as a Thin Plate

6.1 Introduction

Having established the 1-D model of a Kapton film augmented with a PZT bimorph, we now will extend our results to the more practical case of a 2-D structure. We will model the structure as a thin plate under axial loading and assume Kirchhoff's hypotheses hold true. In this chapter, we will derive the weak form of the equations of motion governing the transverse vibrations of a thin plate with attached PZT bimorph. Next, we'll validate the model experimentally. Then, we will formulate the LQR control problem, as well as the 2-D functional gains based on our choice of the Q matrix.

6.2 Model Development using Thin Plate Theory

In this chapter, we will assume that the dynamics of a sheet of Kapton HN material held under tension and augmented with PZT can be modeled as a thin plate. In doing so, we are making the following assumptions: 1) the longitudinal and transverse vibrations are decoupled; 2) the deflections of the surface are small compared to the thickness of the plate; and 3) the tensile term dominates the response of the structure. The third assumption, that the tensile term will dominate the equation of motion, is critical to this analysis because it will add significant stiffness to the system and consequently help validate the second assumption, that the deflections of the system compared to the thickness of the Kapton HN film will be small. We are not modeling the surface as a pure membrane because membrane theory cannot account for the additional stiffness incurred by bonding a PZT actuator to the surface of the structure. However, by treating the surface as a thin plate under a tensile load, we will be able to account for this additional stiffness, consequently giving us a means for introducing the distributed bending moment of a PZT bimorph (or unimorph). Figure 6.1 shows an example geometry of the system under analysis.

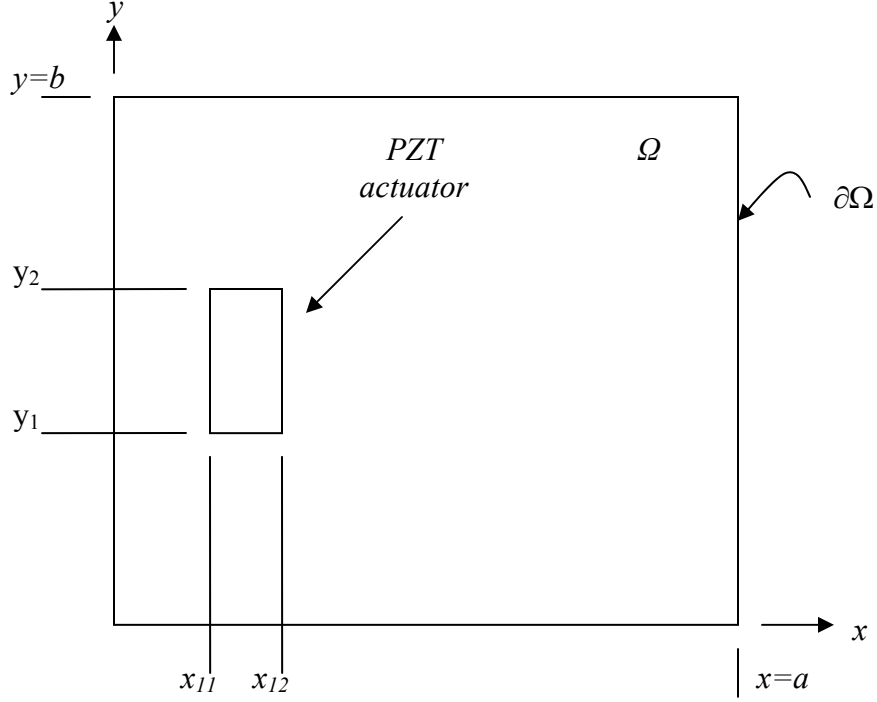


Figure 6.1. Schematic of a generic thin plate's geometry with attached PZT actuators. The coordinates x_{11} , x_{12} , y_1 , and y_2 define the boundary of the actuator, while Ω refers to the domain of the thin plate, and $\partial\Omega$ refers to the boundary of the plate.

6.2.1 Deriving the Weak Form of the Thin Plate Transverse Vibration Equation

The well-known equation governing the transverse dynamics of a thin plate is given by

$$\begin{aligned}
 \rho(x, y)h(x, y) \frac{\partial^2 w(x, y, t)}{\partial t^2} + \frac{\partial^2}{\partial x^2} \left[\frac{E(x, y)[h(x, y)]^3}{12(1-\nu(x, y)^2)} \left[\frac{\partial^2 w(x, y, t)}{\partial x^2} + \nu(x, y) \frac{\partial^2 w(x, y, t)}{\partial y^2} \right] \right] \dots \\
 + \frac{\partial^2}{\partial y^2} \left[\frac{E(x, y)[h(x, y)]^3}{12(1-\nu(x, y)^2)} \left[\frac{\partial^2 w(x, y, t)}{\partial y^2} + \nu(x, y) \frac{\partial^2 w(x, y, t)}{\partial x^2} \right] \right] \dots \\
 + 2 \frac{\partial^2}{\partial x \partial y} \left[\frac{E(x, y)[h(x, y)]^3}{24(1+\nu(x, y))} \left[\frac{\partial^2 w(x, y, t)}{\partial x \partial y} \right] \right] \dots \\
 + 2 \frac{\partial^2}{\partial y \partial x} \left[\frac{E(x, y)[h(x, y)]^3}{24(1+\nu(x, y))} \left[\frac{\partial^2 w(x, y, t)}{\partial y \partial x} \right] \right] = 0.
 \end{aligned} \tag{6.1}$$

In Equation 6.1, $\rho(x,y)$ is the density, $h(x,y)$ is the thickness, $E(x,y)$ is the Young's modulus, $\nu(x,y)$ is Poisson's ratio, and $w(x,y,t)$ is the transverse deflection of the thin plate while undergoing vibration. Next, we wish to augment Equation 6.1 with additional terms to include the effects of viscous air damping, Kelvin-Voigt viscoelastic damping, and the tensile loading in x and y directions. Doing so, we get:

$$\begin{aligned}
& \rho(x,y)h(x,y)\frac{\partial^2 w(x,y,t)}{\partial t^2} + \frac{\partial^2}{\partial x^2} \left[\frac{E(x,y)[h(x,y)]^3}{12(1-\nu(x,y)^2)} \left[\frac{\partial^2 w(x,y,t)}{\partial x^2} + \nu(x,y)\frac{\partial^2 w(x,y,t)}{\partial y^2} \right] \right] \dots \\
& + \frac{\partial^2}{\partial y^2} \left[\frac{E(x,y)[h(x,y)]^3}{12(1-\nu(x,y)^2)} \left[\frac{\partial^2 w(x,y,t)}{\partial y^2} + \nu(x,y)\frac{\partial^2 w(x,y,t)}{\partial x^2} \right] \right] \dots \\
& + 2\frac{\partial^2}{\partial x\partial y} \left[\frac{E(x,y)[h(x,y)]^3}{24(1+\nu(x,y))} \left[\frac{\partial^2 w(x,y,t)}{\partial x\partial y} \right] \right] \dots \\
& + 2\frac{\partial^2}{\partial y\partial x} \left[\frac{E(x,y)[h(x,y)]^3}{24(1+\nu(x,y))} \left[\frac{\partial^2 w(x,y,t)}{\partial y\partial x} \right] \right] \dots \\
& + \gamma \frac{\partial w(x,y,t)}{\partial t} + \frac{\partial^2}{\partial x^2} \left[\frac{\beta(x,y)[h(x,y)]^3}{12(1-\nu(x,y)^2)} \left[\frac{\partial^3 w(x,y,t)}{\partial x^2 \partial t} + \nu(x,y)\frac{\partial^3 w(x,y,t)}{\partial y^2 \partial t} \right] \right] \dots \\
& + \frac{\partial^2}{\partial y^2} \left[\frac{\beta(x,y)[h(x,y)]^3}{12(1-\nu(x,y)^2)} \left[\frac{\partial^3 w(x,y,t)}{\partial y^2 \partial t} + \nu(x,y)\frac{\partial^3 w(x,y,t)}{\partial x^2 \partial t} \right] \right] \dots \\
& + 2\frac{\partial^2}{\partial x\partial y} \left[\frac{\beta(x,y)[h(x,y)]^3}{24(1+\nu(x,y))} \left[\frac{\partial^3 w(x,y,t)}{\partial x\partial y \partial t} \right] \right] \dots \\
& + 2\frac{\partial^2}{\partial y\partial x} \left[\frac{\beta(x,y)[h(x,y)]^3}{24(1+\nu(x,y))} \left[\frac{\partial^3 w(x,y,t)}{\partial y\partial x \partial t} \right] \right] \dots \\
& + Px \frac{\partial^2 w(x,y,t)}{\partial x^2} + Py \frac{\partial^2 w(x,y,t)}{\partial y^2} = 0.
\end{aligned} \tag{6.2}$$

In Equation 6.2, γ is the viscous air damping parameter, $\beta(x,y)$ is the Kelvin-Voigt proportional damping parameter, and Px and Py refer to tensile loads in the x and y directions, respectively. Equation 6.2, with the appropriate boundary conditions, governs

the damped transverse dynamics of a thin plate with applied tensile loading undergoing free vibration. We can rewrite Equation 6.2 more compactly as:

$$\begin{aligned} \rho h w_{tt} + [D[w_{xx} + \nu w_{yy}]_{xx} + [D[w_{yy} + \nu w_{xx}]_{yy} + 2[Gw_{xy}]_{xy} + 2[Gw_{yx}]_{yx} \\ + \gamma w_t + [D_\beta[w_{xxt} + \nu w_{yyt}]_{xx} + [D_\beta[w_{yyt} + \nu w_{xxt}]_{yy} \\ + 2[G_\beta w_{xyt}]_{xy} + 2[G_\beta w_{yxt}]_{yx} + (Px)w_{xx} + (Py)w_{yy} = 0, \end{aligned} \quad (6.3)$$

where

$$D = \frac{Eh^3}{12(1-\nu^2)}, \quad G = \frac{Eh^3}{24(1+\nu)}, \quad D_\beta = \frac{\beta h^3}{12(1-\nu^2)}, \quad G_\beta = \frac{\beta h^3}{24(1+\nu)}. \quad (6.4)$$

In Equations 6.4, D is the flexural stiffness of the thin plate and G is the rigidity, or resistance to shearing, of the thin plate. The subscripts x , y , and t are spatial or temporal derivatives of the particular term, as defined in previous chapters. The subscript β is used to distinguish the Kelvin-Voigt viscoelastic damping terms from the structural elastic terms.

Next we wish to put Equation 6.3 into weak form so that we can approximate the system dynamics using finite elements, or more specifically, cubic B-splines. To do so, we follow a similar procedure as outlined previously in Chapters 3 and 4. First, we need to place the system dynamics in first order form. In doing so, we define two states for our system dynamics, position $d(x,y,t)$ and velocity $v(x,y,t)$, and have

$$\begin{aligned} d_t = v \\ \rho h v_t = -[D[d_{xx} + \nu d_{yy}]_{xx} - [D[d_{yy} + \nu d_{xx}]_{yy} - 2[Gd_{xy}]_{xy} - 2[Gd_{yx}]_{yx} \dots \\ - \gamma v - [D_\beta[v_{xx} + \nu v_{yy}]_{xx} - [D_\beta[v_{yy} + \nu v_{xx}]_{yy} \dots \\ - 2[G_\beta v_{xy}]_{xy} - 2[G_\beta v_{yx}]_{yx} - (Px)d_{xx} - (Py)d_{yy} = 0. \end{aligned} \quad (6.5)$$

Next, as in the 1-D case, we multiply through by test functions $\phi(x,y)$ and $\psi(x,y)$ and integrate over the domain of the plate, Ω . Following these steps, we get

$$\begin{aligned}
 \int_{\Omega} d_i \phi d\Omega &= \int_{\Omega} v \phi d\Omega \\
 \int_{\Omega} \rho h v_i \psi d\Omega &= - \int_{\Omega} \left\{ [D[d_{xx} + \nu d_{yy}]]_{xx} + [D[d_{yy} + \nu d_{xx}]]_{yy} + 2[Gd_{xy}]_{xy} + 2[Gd_{yx}]_{yx} \dots \right. \\
 &\quad + \gamma v + [D_{\beta}[v_{xx} + \nu v_{yy}]]_{xx} + [D_{\beta}[v_{yy} + \nu v_{xx}]]_{yy} \dots \\
 &\quad \left. + 2[G_{\beta}v_{xy}]_{xy} + 2[G_{\beta}v_{yx}]_{yx} + (Px)d_{xx} + (Py)d_{yy} \right\} \psi d\Omega = 0.
 \end{aligned} \tag{6.6}$$

The integration of Equation 6.6 requires a significant amount of attention to arrive at the weak form. Here we will introduce the 2-D Divergence theorem in Cartesian coordinates, which states that:

$$\int_{\Omega} u \frac{\partial w}{\partial x} d\Omega = \int_{\partial\Omega} (uw) dy - \int_{\Omega} w \frac{\partial u}{\partial x} d\Omega \tag{6.7}$$

and

$$\int_{\Omega} u \frac{\partial w}{\partial y} d\Omega = - \int_{\partial\Omega} (uw) dx - \int_{\Omega} w \frac{\partial u}{\partial y} d\Omega . \tag{6.8}$$

In Equations 6.7 and 6.8, $d\Omega = dx dy$, $\partial\Omega$ is the plate's boundary, and Ω is the interior region of the plate.

Starting from the second line of Equation 6.6, we will step through the integration process of the right hand side of the equality term by term using the Divergence theorem. Accordingly, we have:

$$\begin{aligned}
\int_{\Omega} [D[d_{xx} + \nu d_{yy}]_{xx}] \psi d\Omega &= \int_{\partial\Omega} [D[d_{xx} + \nu d_{yy}]_x] \psi dy - \int_{\partial\Omega} [D[d_{xx} + \nu d_{yy}]_y] \psi_x dy \dots \\
&+ \int_{\Omega} [D[d_{xx} + \nu d_{yy}]_{xx}] \psi_{xx} d\Omega
\end{aligned} \tag{6.9}$$

$$\begin{aligned}
\int_{\Omega} [D[d_{yy} + \nu d_{xx}]_{yy}] \psi d\Omega &= - \int_{\partial\Omega} [D[d_{yy} + \nu d_{xx}]_y] \psi dx - \int_{\partial\Omega} [D[d_{yy} + \nu d_{xx}]_x] \psi_y dx \\
&+ \int_{\Omega} [D[d_{yy} + \nu d_{xx}]_{yy}] \psi_{yy} d\Omega
\end{aligned} \tag{6.10}$$

$$\begin{aligned}
\int_{\Omega} [2G[d_{xy}]_{xy}] \psi d\Omega &= - \int_{\partial\Omega} [2G[d_{xy}]_x] \psi dx - \int_{\partial\Omega} [2G[d_{xy}]_y] \psi_y dy \dots \\
&+ \int_{\Omega} [2G[d_{xy}]_{xy}] \psi_{xy} d\Omega
\end{aligned} \tag{6.11}$$

$$\begin{aligned}
\int_{\Omega} [2G[d_{yx}]_{yx}] \psi d\Omega &= \int_{\partial\Omega} [2G[d_{yx}]_y] \psi dy + \int_{\partial\Omega} [2G[d_{yx}]_x] \psi_x dx \dots \\
&+ \int_{\Omega} [2G[d_{yx}]_{yx}] \psi_{yx} d\Omega
\end{aligned} \tag{6.12}$$

$$\int_{\Omega} \gamma \nu \psi d\Omega = \int_{\Omega} \gamma \nu \psi d\Omega \tag{6.13}$$

$$\begin{aligned}
\int_{\Omega} [D_{\beta} [\nu_{xx} + \nu \nu_{yy}]_{xx}] \psi d\Omega &= \int_{\partial\Omega} [D_{\beta} [\nu_{xx} + \nu \nu_{yy}]_x] \psi dy - \int_{\partial\Omega} [D_{\beta} [\nu_{xx} + \nu \nu_{yy}]_y] \psi_x dy \dots \\
&+ \int_{\Omega} [D_{\beta} [\nu_{xx} + \nu \nu_{yy}]_{xx}] \psi_{xx} d\Omega
\end{aligned} \tag{6.14}$$

$$\begin{aligned}
\int_{\Omega} [D_{\beta} [\nu_{yy} + \nu \nu_{xx}]_{yy}] \psi d\Omega &= - \int_{\partial\Omega} [D_{\beta} [\nu_{yy} + \nu \nu_{xx}]_y] \psi dx - \int_{\partial\Omega} [D_{\beta} [\nu_{yy} + \nu \nu_{xx}]_x] \psi_y dx \dots \\
&+ \int_{\Omega} [D_{\beta} [\nu_{yy} + \nu \nu_{xx}]_{yy}] \psi_{yy} d\Omega
\end{aligned} \tag{6.15}$$

$$\begin{aligned}
\int_{\Omega} [2G_{\beta} [v_{xy}]_{xy}] \psi d\Omega &= - \int_{\partial\Omega} [2G_{\beta} [v_{xy}]_x] \psi dx - \int_{\partial\Omega} [2G_{\beta} [v_{xy}]_y] \psi dy \dots \\
&+ \int_{\Omega} [2G_{\beta} [v_{xy}]] \psi_{xy} d\Omega
\end{aligned} \tag{6.16}$$

$$\begin{aligned}
\int_{\Omega} [2G_{\beta} [v_{yx}]_{yx}] \psi d\Omega &= \int_{\partial\Omega} [2G_{\beta} [v_{yx}]_y] \psi dy + \int_{\partial\Omega} [2G_{\beta} [v_{yx}]_x] \psi dx \dots \\
&+ \int_{\Omega} [2G_{\beta} [v_{yx}]] \psi_{yx} d\Omega
\end{aligned} \tag{6.17}$$

$$\int_{\Omega} [Px [d_x]_x] \psi d\Omega = \int_{\partial\Omega} [Px [d_x]] \psi dy - \int_{\partial\Omega} [Px [d_x]] \psi_x d\Omega \tag{6.18}$$

and finally,

$$\int_{\Omega} [Py [d_y]_y] \psi d\Omega = - \int_{\partial\Omega} [Py [d_y]] \psi dx - \int_{\partial\Omega} [Py [d_y]] \psi_y d\Omega. \tag{6.19}$$

Now that we've evaluated these integrals, we can separate the resultants into boundary integrals and the equation governing the dynamics of the transverse vibrations of the thin plate. First, we have the boundary integrals, namely:

$$\begin{aligned}
&\int_{\partial\Omega} [D [d_{xx} + \nu d_{yy}]_x] \psi dy - \int_{\partial\Omega} [D [d_{xx} + \nu d_{yy}]_y] \psi_x dy - \int_{\partial\Omega} [D [d_{yy} + \nu d_{xx}]_y] \psi dx \dots \\
&- \int_{\partial\Omega} [D [d_{yy} + \nu d_{xx}]_x] \psi_y dx - \int_{\partial\Omega} [2G [d_{xy}]_x] \psi dx - \int_{\partial\Omega} [2G [d_{xy}]_y] \psi_y dy \dots \\
&\int_{\partial\Omega} [2G [d_{yx}]_y] \psi dy + \int_{\partial\Omega} [2G [d_{yx}]_x] \psi_x dx + \int_{\partial\Omega} [D_{\beta} [v_{xx} + \nu v_{yy}]_x] \psi dy - \int_{\partial\Omega} [D_{\beta} [v_{xx} + \nu v_{yy}]_y] \psi_x dy \dots \\
&- \int_{\partial\Omega} [D_{\beta} [v_{yy} + \nu v_{xx}]_y] \psi dx - \int_{\partial\Omega} [D_{\beta} [v_{yy} + \nu v_{xx}]_x] \psi_y dx - \int_{\partial\Omega} [2G_{\beta} [v_{xy}]_x] \psi dx \dots \\
&- \int_{\partial\Omega} [2G_{\beta} [v_{xy}]_y] \psi_y dy + \int_{\partial\Omega} [2G_{\beta} [v_{yx}]_y] \psi dy + \int_{\partial\Omega} [2G_{\beta} [v_{yx}]_x] \psi_x dx + \int_{\partial\Omega} [Px [d_x]] \psi dy \dots \\
&- \int_{\partial\Omega} [Py [d_y]] \psi dx.
\end{aligned} \tag{6.20}$$

Secondly, we have

$$\begin{aligned}
\frac{\partial}{\partial t} \int_{\Omega} \rho h v \psi \, d\Omega = & - \int_{\Omega} \left\{ \left[D \left[d_{xx} + \nu d_{yy} \right] \right] \psi_{xx} + \left[D \left[d_{yy} + \nu d_{xx} \right] \right] \psi_{yy} + 2 \left[G d_{xy} \right] \psi_{xy} + 2 \left[G d_{yx} \right] \psi_{yx} \dots \right. \\
& + \gamma v \psi + \left[D_{\beta} \left[v_{xx} + \nu v_{yy} \right] \right] \psi_{xx} + \left[D_{\beta} \left[v_{yy} + \nu v_{xx} \right] \right] \psi_{yy} \dots \\
& \left. + 2 \left[G_{\beta} v_{xy} \right] \psi_{xy} + 2 \left[G_{\beta} v_{yx} \right] \psi_{yx} + (Px) d_x \psi_x + (Py) d_y \psi_y \right\} d\Omega = 0
\end{aligned} \tag{6.21}$$

Equation 6.21 is the weak form of the dynamic equation governing the transverse vibrations of the plate. Now, we wish to introduce our approximations. In a similar fashion to our 1-D equations, we will approximate our states using finite elements, and more specifically in our case, cubic B-splines. Therefore, we have:

$$d(x, y, t) = \sum_{i=1}^N d_i(t) \psi_i(x, y) \tag{6.22}$$

and

$$v(x, y, t) = \sum_{i=1}^N v_i(t) \psi_i(x, y). \tag{6.23}$$

Plugging our approximations into Equation 6.21 yields

$$\begin{aligned}
& \frac{\partial}{\partial t} \sum_{i=1}^N v_i \int_{\Omega} \rho h \psi_i \psi_j d\Omega = - \sum_{i=1}^N d_i \int_{\Omega} [D((\psi_i)_{xx} + v(\psi_i)_{yy})](\psi_j)_{xx} d\Omega \dots \\
& - \sum_{i=1}^N d_i \int_{\Omega} [D((\psi_i)_{yy} + v(\psi_i)_{xx})](\psi_j)_{yy} d\Omega - \sum_{i=1}^N d_i \int_{\Omega} [2G((\psi_i)_{xy})](\psi_j)_{xy} d\Omega \\
& - \sum_{i=1}^N d_i \int_{\Omega} [2G((\psi_i)_{yx})](\psi_j)_{yx} d\Omega - \sum_{i=1}^N v_i \int_{\Omega} \gamma \psi_i \psi_j d\Omega - \sum_{i=1}^N v_i \int_{\Omega} [D_{\beta}((\psi_i)_{xx} + v(\psi_i)_{yy})](\psi_j)_{xx} d\Omega \dots \\
& - \sum_{i=1}^N v_i \int_{\Omega} [D_{\beta}((\psi_i)_{yy} + v(\psi_i)_{xx})](\psi_j)_{yy} d\Omega - \sum_{i=1}^N v_i \int_{\Omega} [2G_{\beta}((\psi_i)_{xy})](\psi_j)_{xy} d\Omega \dots \\
& \sum_{i=1}^N v_i \int_{\Omega} [2G_{\beta}((\psi_i)_{yx})](\psi_j)_{yx} d\Omega - \sum_{i=1}^N d_i \int_{\Omega} [Px((\psi_i)_x)](\psi_j)_x d\Omega - \sum_{i=1}^N d_i \int_{\Omega} [Py((\psi_i)_y)](\psi_j)_y d\Omega = 0
\end{aligned} \tag{6.24}$$

Finally, we arrive at the approximated weak form of the governing dynamical equation. As was the case in the 1-D structure, we can define the following matrices to help make our notation more compact:

$$[M_1]_{i,j=1}^N = \int_{\Omega} \psi_i \psi_j d\Omega \tag{6.25}$$

$$[M_2]_{i,j=1}^N = \int_{\Omega} \rho h \psi_i \psi_j d\Omega \tag{6.26}$$

$$[K_2]_{i,j=1}^N = \int_{\Omega} [D((\psi_i)_{xx} + v(\psi_i)_{yy})](\psi_j)_{xx} d\Omega \tag{6.27}$$

$$[K_2]_{i,j=1}^N = \int_{\Omega} [D((\psi_i)_{yy} + v(\psi_i)_{xx})](\psi_j)_{yy} d\Omega \tag{6.28}$$

$$[K_3]_{i,j=1}^N = \int_{\Omega} [2G((\psi_i)_{xy})](\psi_j)_{xy} d\Omega \tag{6.29}$$

$$[K_4]_{i,j=1}^N = \int_{\Omega} [2G((\psi_i)_{yx})](\psi_j)_{yx} d\Omega \tag{6.30}$$

$$[K_5]_{i,j=1}^N = \int_{\Omega} [Px((\psi_i)_x)](\psi_j)_x + [Py((\psi_i)_y)](\psi_j)_y d\Omega \tag{6.31}$$

$$[C_1]_{i,j=1}^N = \int_{\Omega} [D_{\beta} ((\psi_i)_{xx} + \nu(\psi_i)_{yy})] (\psi_j)_{xx} d\Omega \quad (6.32)$$

$$[C_2]_{i,j=1}^N = \int_{\Omega} [D_{\beta} ((\psi_i)_{yy} + \nu(\psi_i)_{xx})] (\psi_j)_{yy} d\Omega \quad (6.33)$$

$$[C_3]_{i,j=1}^N = \int_{\Omega} [2G_{\beta} ((\psi_i)_{xy})] (\psi_j)_{xy} d\Omega \quad (6.34)$$

$$[C_4]_{i,j=1}^N = \int_{\Omega} [2G_{\beta} ((\psi_i)_{yx})] (\psi_j)_{yx} d\Omega. \quad (6.35)$$

By letting $\bar{d} = [d_i(t)]_{i=1}^N$ and $\bar{v} = [v_i(t)]_{i=1}^N$, we can rewrite our system equations as:

$$\begin{bmatrix} M_1 & 0 \\ 0 & M_2 \end{bmatrix} \begin{bmatrix} \bar{d} \\ \bar{v} \end{bmatrix}_t = \begin{bmatrix} 0 & M_1 \\ -K_1 - K_2 - K_3 - K_4 - K_5 & -C_1 - C_2 - C_3 - C_4 - \gamma M_1 \end{bmatrix} \begin{bmatrix} \bar{d} \\ \bar{v} \end{bmatrix} \quad (6.36)$$

6.2.2 Including the 2-D Effects of a PZT Bimorph in the System Dynamics

Equation 6.36 is an approximation to the system dynamics of a thin plate undergoing transverse vibration. Our next goal is to integrate the dynamics of a PZT bimorph patch into the equation of motion. The addition of a PZT bimorph will add significant mass and stiffness to the system and must be accounted for in our dynamical formulation. Further, the electromechanical coupling of the PZT bimorph will allow us to link an applied control voltage to our system to eliminate any detrimental vibration.

The derivation of the bending actuation induced by our PZT bimorphs is similar to the derivation presented in Chapter 5 and is based on the derivation as presented by Banks, Smith, and Wang (1996). However, unlike the derivation presented in Chapter 5, we must now account for the actuation in the *y-direction*, and take into account Poisson's

effect as the actuator deforms the membrane film. As before, we begin by assuming that the induced external stress is given by

$$(\sigma_x)_i = \frac{E_{pzt}}{1 - \nu_{pzt}} \frac{d_{31}}{h_{pzt}} V_i. \quad (6.37)$$

Here, E_{pzt} is the Young's modulus of the piezoelectric material, d_{31} is the electromechanical coupling coefficient of the piezoelectric material, h_{pzt} is the thickness, ν_{pzt} is the Poisson's ratio, and V_i is the applied voltage to the patch. The subscript i refers to either *patch 1* or *patch 2* of a bimorph. A similar expression is assumed for stresses induced in the *y-direction*. Integrating Equation 6.37 through the thickness of a unit element, we obtain an expression for the total external force resultant, namely,

$$(M_x)_i = \int_{h/2}^{h/2+h_{pzt}} (\sigma_x)_i z dz. \quad (6.38)$$

The units given by Equation 6.38 are $\frac{N \cdot m}{m}$. Plugging Equation 6.37 into Equation 6.38 and performing the integration yields the following expression for the force resultant applied to the surface by the actuator:

$$(M_x)_i = -\frac{E_{pzt}}{1 - \nu_{pzt}} \left[\frac{1}{8} \left(4 \left(\frac{h}{2} + h_{pzt} \right)^2 \right) \right] \frac{d_{31}}{h_{pzt}} V_i. \quad (6.39)$$

Similarly, for actuation in the *y-direction*, we have

$$(M_y)_i = -\frac{E_{pzt}}{1 - \nu_{pzt}} \left[\frac{1}{8} \left(4 \left(\frac{h}{2} + h_{pzt} \right)^2 \right) \right] \frac{d_{31}}{h_{pzt}} V_i. \quad (6.40)$$

The equations for the contributed moment from the other half of the PZT bimorph are found by integrating through the thickness of the structure in the opposite direction, thus producing an equivalent magnitude to Equations 6.39 and 6.40 but with opposite polarity. To account for the finite actuation regions on the surface of the membrane film, we will again use the $\chi(x,y)$ function, where

$$\chi(x,y) = \begin{cases} 1 & x_{11} \leq x \leq x_{12} \text{ and } y_1 \leq y \leq y_2 \\ \text{if} & \\ 0 & \text{otherwise} \end{cases} . \quad (6.41)$$

Consequently, for each PZT bimorph, we have

$$(M_x)_{combined} = [(M_x)_1 + (M_x)_2] \chi(x,y) \quad (6.42)$$

and

$$(M_y)_{combined} = [(M_y)_1 + (M_y)_2] \chi(x,y). \quad (6.43)$$

To excite the transverse modes of the thin plate, the two PZT patches for a particular bimorph are excited out-of-phase. Conversely, if one wishes to excite the in-plane modes only, the patches of a particular bimorph should be excited in-phase.

Since we have defined the $\chi(x,y)$ function, we should also note the additional mass, stiffness, and damping effects introduced into the equations of motion for the system due to the addition of the PZT bimorphs. Accordingly, we have:

$$\begin{aligned} D(x,y) &= D_{plate}(x,y) + D_{pzt} \chi(x,y), \\ G(x,y) &= G_{plate}(x,y) + G_{pzt} \chi(x,y), \\ D_\beta(x,y) &= (D_\beta(x,y))_{plate} + [(D_\beta(x,y))_{pzt}] \chi(x,y), \\ G_\beta(x,y) &= (G_\beta(x,y))_{plate} + [(G_\beta(x,y))_{pzt}] \chi(x,y) \end{aligned} \quad (6.44)$$

where the contributions from the piezoelectric material are given by

$$\begin{aligned}
D_{pzt}(x, y) &= \frac{2E_{pzt} \left[\left(\frac{h}{2} + h_{pzt} \right)^3 - \frac{h^3}{8} \right]}{3(1 - \nu_{pzt}^2)}, \\
G_{pzt}(x, y) &= \frac{E_{pzt} \left[\left(\frac{h}{2} + h_{pzt} \right)^3 - \frac{h^3}{8} \right]}{3(1 + \nu_{pzt})}, \\
(D_{\beta}(x, y))_{pzt} &= \frac{2\beta_{pzt} \left[\left(\frac{h}{2} + h_{pzt} \right)^3 - \frac{h^3}{8} \right]}{3(1 - \nu_{pzt}^2)}, \\
(G_{\beta}(x, y))_{pzt} &= \frac{\beta_{pzt} \left[\left(\frac{h}{2} + h_{pzt} \right)^3 - \frac{h^3}{8} \right]}{3(1 + \nu_{pzt})}.
\end{aligned} \tag{6.45}$$

6.3 Baseline Membrane Testing

Before an investigation into the proper modeling of a 2-D membrane augmented with active piezoelectric material was carried out, a baseline test on a Kapton membrane was performed. The goals of this baseline test were to: 1) establish the pre-stress in the Kapton material in both the x and y -directions and 2) to provide a reference for understanding from a physical standpoint the consequences of adding active material to the membrane. The following sections briefly describe the experimental setup, analysis, and results of the baseline testing.

6.3.1 Baseline Testing Experimental Procedure

A pre-stressed Kapton HN membrane sample (51 μ m thick) was glued to a piece of 1/2" thick acrylic using a 3M spray adhesive. To properly adhere the Kapton to the acrylic, a 30 lb. weight was placed on top of the acrylic, pressing the spray adhesive and membrane together evenly on a hard surface. The central region of the acrylic, cut out to form an

area 127 mm x 152 mm (5" x 6"), formed the membrane's domain. The adhered edges of the membrane provided a fixed boundary condition.

Once the Kapton was adhered to the acrylic, a 5 x 4 grid was marked on the surface of the membrane to specify dynamic measurement locations. One of the known difficulties in testing of membrane structures is providing proper excitation for dynamic analysis. More traditional techniques, like using an electromechanical shaker with a mechanical attachment point to the membrane, cause exaggerated localized vibration and considerable mass loading effect—both of which are detrimental to accurate system identification. To bypass these inadequacies, an excitation technique based on magnetic field interaction was used. First, a small piece of permanent magnet material (1 cm x 1 cm) was attached with double-sided tape to the front side of the membrane. Although the added piece of magnetic material does exhibit a localized mass loading effect, the effect is relatively small when compared to the alternative of using a traditional electromagnetic shaker and stinger.

The electromagnet was positioned in front of the small magnet of the membrane. By driving the electromagnet with a frequency-varying, sinusoidal wave via an HP Bipolar Power Supply, the developed magnetic field at the tip of the electromagnet produced an attractive / repulsive force between the two magnets. Consequently, the membrane could be driven with a known sinusoidal input, from which we could measure the velocity response of the membrane using the Polytec laser vibrometer. The test was performed within the Tenney environmental chamber at 10 torr. Such near-vacuum conditions ensure that membrane theory can be used while neglecting any air mass loading effects. A picture of the experimental setup is shown in Figure 6.2. A schematic of the experimental setup is shown in Figure 6.3.

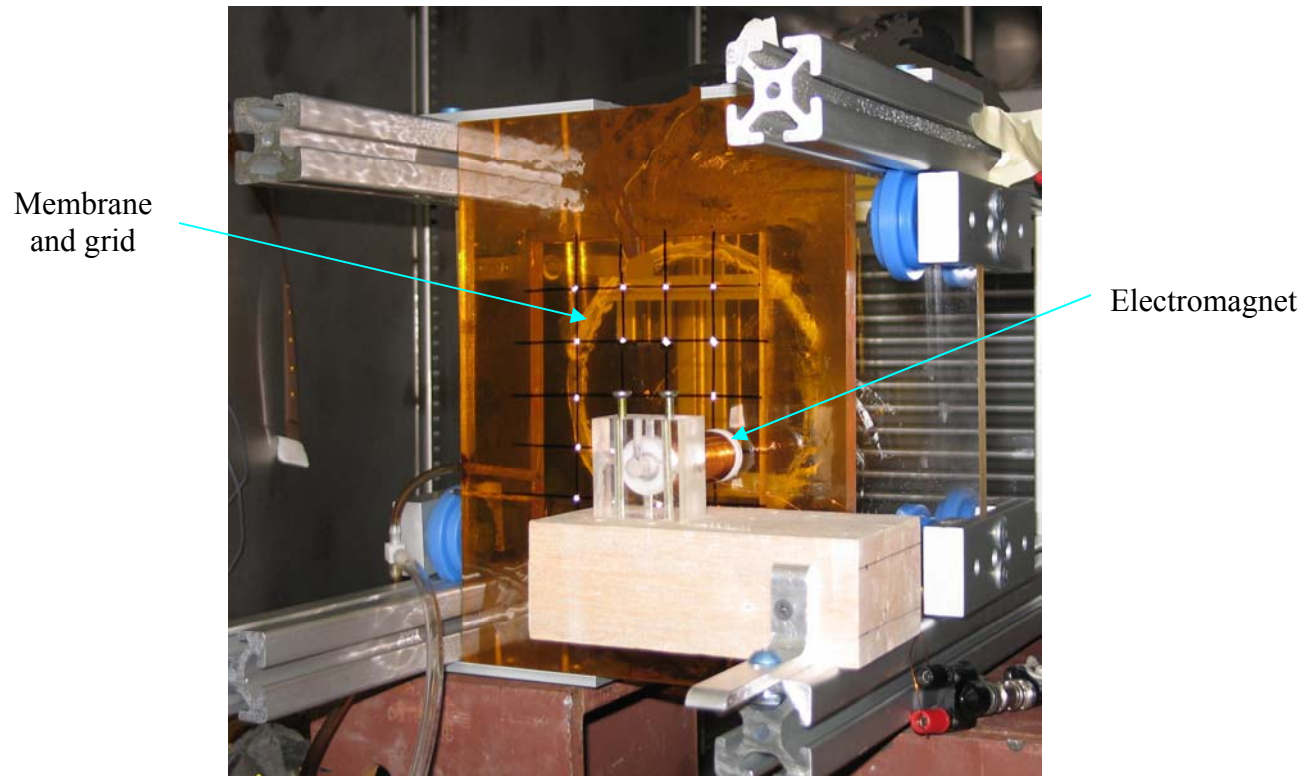


Figure 6.2. Photograph of the baseline membrane dynamic test setup. The Kapton membrane, glued to a sheet of acrylic with a 127 mm x 152 mm rectangular cutout, was dynamically excited using an electromagnet.

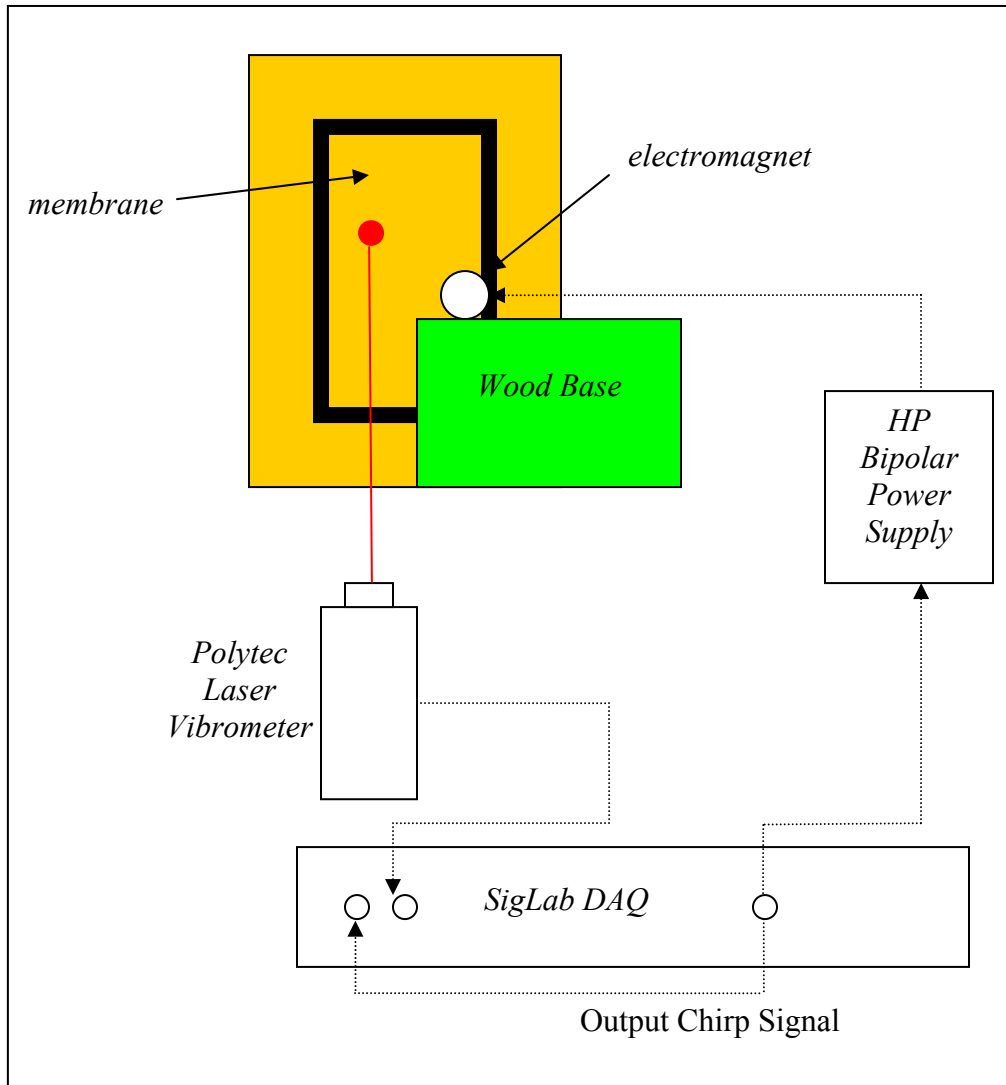


Figure 6.3. Schematic diagram of the experimental setup using an electromagnet to dynamically excite a Kapton membrane.

6.3.2 Dynamic Analysis of the Baseline Membrane

A sample frequency response function of the membrane is shown in Figure 6.4. The dynamics of the electromagnet force generated as a result of the current applied have been documented by Sodano (2005) as having a break frequency at 15 Hz and a 20 dB/decade rolloff thereafter. Within the excitation bandwidth of the current experiment, exciting from 50 – 300 Hz, the minimal force required to excite the membrane within this frequency range allows the electromagnet to be an effective actuator.

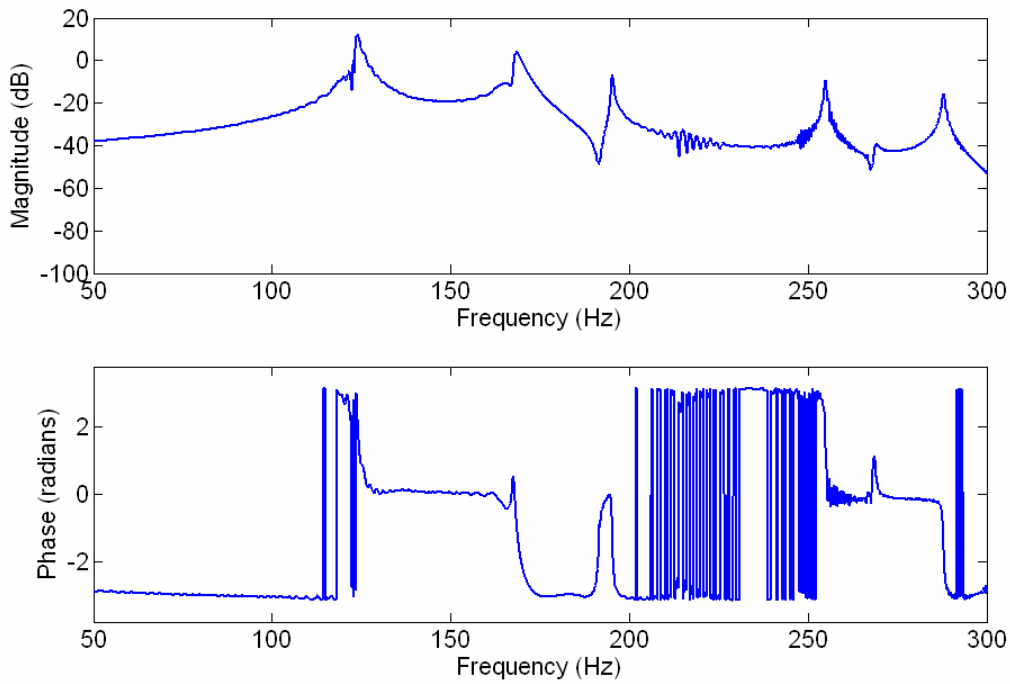


Figure 6.4. Experimentally measured transfer function of the Kapton membrane, measured (from the bottom left corner of Figure 6.2) at a point 2” along the x -axis and 3” along the y -axis.

As shown in the Figure 6.4, the first few resonant peaks of the membrane occur at 123, 167, 194, 254, 267, and 288 Hz. From these experimentally determined frequencies, we can then use membrane theory to identify the pre-stress in the membrane.

Using the first identified resonant peak of the membrane at 167 Hz, and assuming that the tensile load is uniform in both principle axes, the tensile load can be analytically determined by the equation (Meirovitch, 1997)

$$T = \frac{(2f_1)^2 \sigma}{\left(\frac{1}{a^2} + \frac{1}{b^2}\right)}, \quad (6.46)$$

where σ is the mass per unit area, a is the length in the x -direction, and b is the length in the y -direction. Using the material properties of Kapton HN and the dimensions of the

test setup, the calculated tensile loading in the membrane is 40.6 N/m. Under this tensile load, the resonant frequencies of the membrane up to 300 Hz can be calculated and compared to the measured frequencies of the system (as shown in Table 6.1).

Table 6.1. Comparison between the experimentally determined frequencies of the Kapton membrane and those calculated using pure membrane theory.

Mode #	Experiment	Analytic	% Error
	Frequency (Hz)	Frequency (Hz)	
1	123	123	0.0
2	167	183	-9.6
3	194	204	-5.2
4	254	245	3.5
5	267	254	4.9

Although the assumption that the tensile loading applied in both principle axis directions is uniform is an idealization, the analytical model predicts the first five resonant frequencies of the Kapton membrane by an average error of 6%. Using a finite element model with 2-D linear hat functions, we can find an approximation to the eigenvalues of a membrane under uniform loading. The converged finite element model consists of a mesh of 20 x 24 elements, for a total of 480 elements. A comparison between the analytically determined resonant frequencies and the FE model predicted frequencies is shown in Table 6.2.

Table 6.2. Comparison between the analytical and FEM frequencies of the Kapton membrane.

Mode #	Analytic	FEM	% Error
	Frequency (Hz)	Frequency (Hz)	
1	123	122.1	0.7
2	183	182.6	0.2
3	204	203.8	0.1
4	245	244.9	0.0
5	254	253.8	0.1

As shown by Table 6.2, the converged FE model is within 1% of the analytically determined frequencies of the membrane system. Consequently, we can use the converged FE model in later sections as an analysis tool.

6.4 Experimental Validation of the Finite Element Model

Having rigorously defined the finite element framework for the proposed membrane lens using thin plate theory, and then having performed an experiment to determine the dynamic properties of a Kapton membrane, we will next design an experiment to see how well the proposed thin plate theory agrees with a true active membrane system. As in Chapter 5, the piezoelectric bimorph will be constructed from H4 series PZT. A summary of the important material and geometric properties is given in Table 6.3.

Table 6.3. Summary of nominal material properties of the Kapton HN material and the PZT bimorph actuator.

	Parameter	Symbol	Value
Kapton HN	modulus	E	165 MPa
	length	a	0.127 m
	width	b	0.152 m
	thickness	h	51 μm
	density	ρ	1400 kg/m^3
	viscous air damping	γ	0.02
	Poisson's ratio	ν	0.34
H4 PZT Wafer	coupling coefficient	d_{31}	4.2 pm/V
	modulus	E_{pzt}	62 GPa
	bimorph 1	x_{11}	0.052 m
	bimorph 1	x_{12}	0.078 m
	bimorph 1	y_1	0.102 m
	bimorph 1	y_2	0.133 m
	patch thickness	h_{pzt}	533.4 μm
	density	ρ_{pzt}	7800 kg/m^3
	Poisson's ratio	ν_{pzt}	0.31

Next, we will discuss the experimental setup used to validate modeling the system with thin plate theory. These test results will show that the use of thin plate theory is valid and

that membrane theory that takes into account variable mass densities throughout the structure is inadequate for capturing the relevant structural dynamics.

6.4.1 Experimental Setup and Hardware

The experimental setup consists of a 127 mm x 152 mm sample of Kapton HN (51 μm thick). Two wafers of H4 piezoelectric material (25 mm x 32 mm) were glued to the membrane sample to serve as the excitation actuator for the system. Copper tape was used as the conductive layer on one side of the H4 PZT wafer to attach one lead wire, and a second lead wire was attached to the opposite side of the PZT wafer using SuperSafe Superior #30 Soft Solder Flux Liquid. A diagram of the membrane with attached PZT bimorph is shown in Figure 6.5.

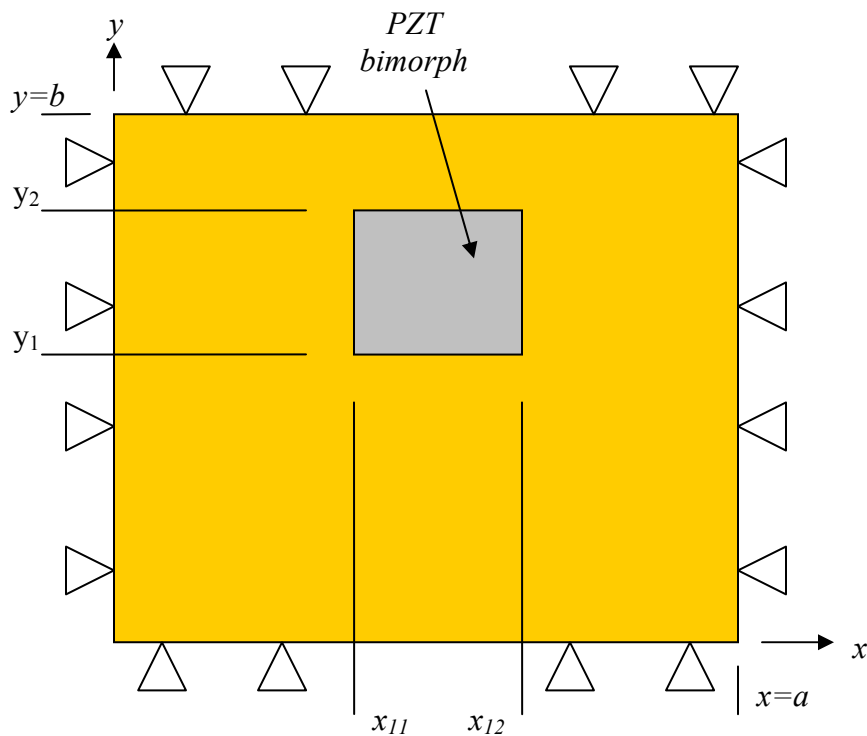


Figure 6.5. A diagram of the experimental setup. All four boundaries are assumed to be fixed.

All four boundary conditions, as shown in Figure 6.5, are assumed to be fixed. A photograph of the actual experimental membrane is shown in Figure 6.6. A schematic of the experimental setup, including relevant hardware, is shown in Figure 6.7.

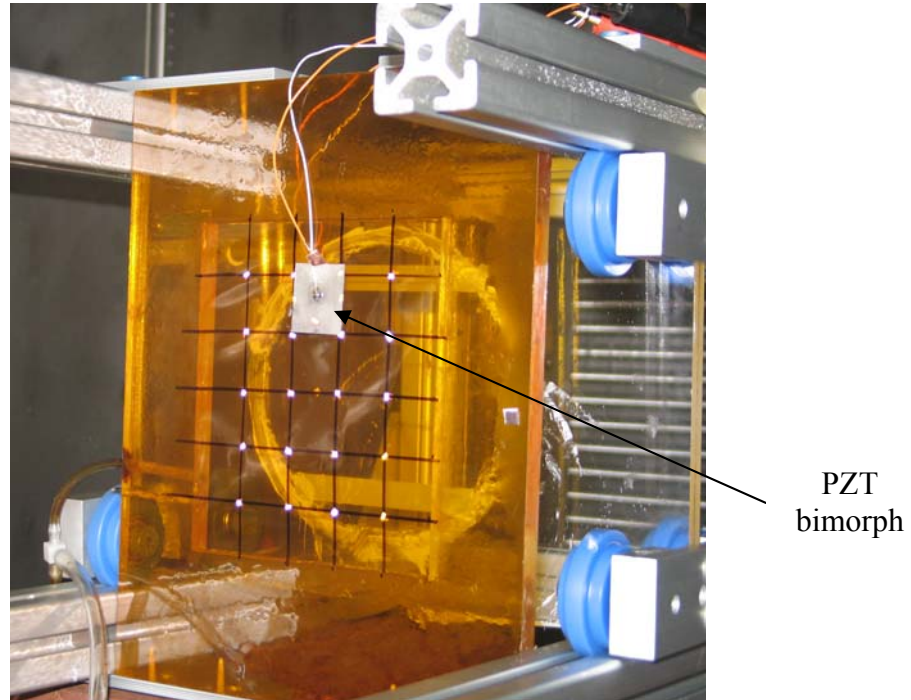


Figure 6.6. Photograph of the experimental setup of the membrane with active PZT bimorph.

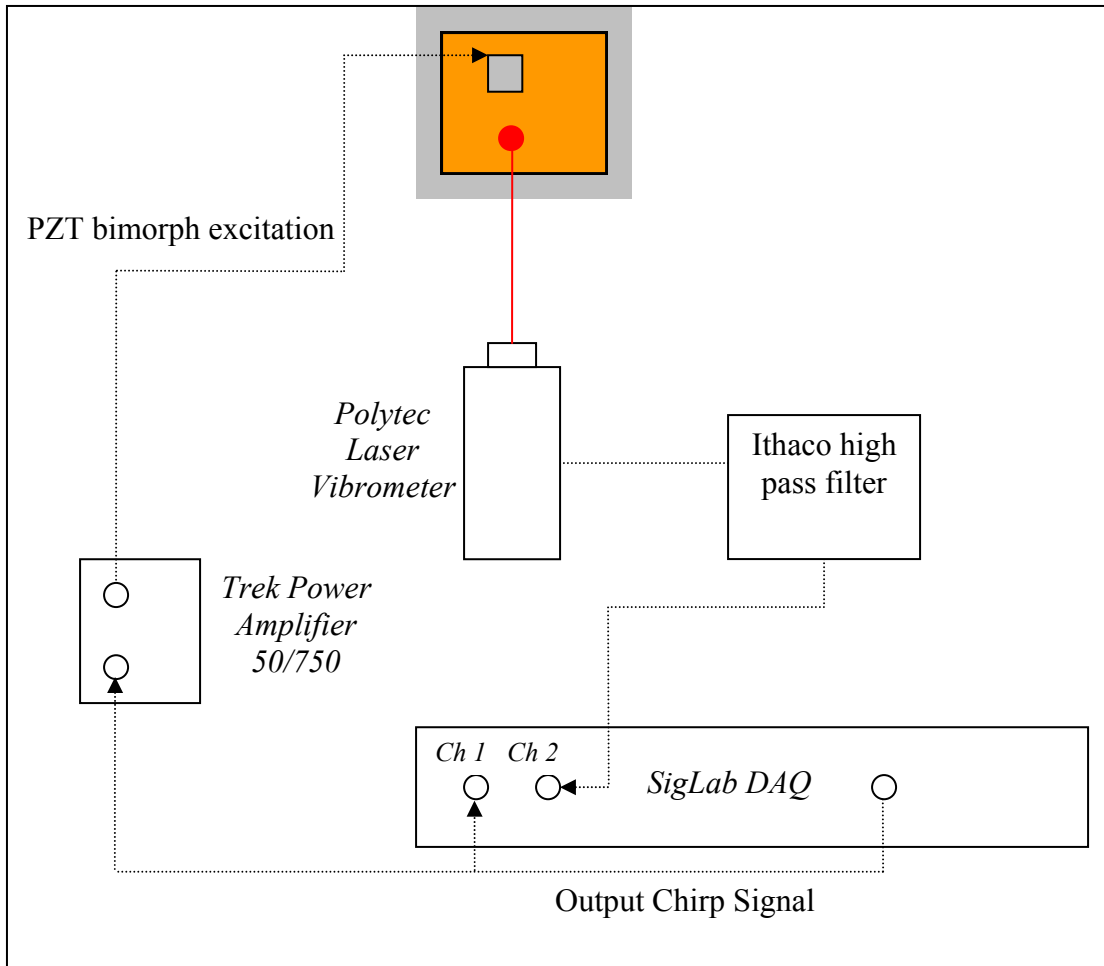


Figure 6.7. Schematic drawing of the experimental setup for PZT bimorph excitation of the membrane.

6.4.2 Data Acquisition

The excitation signal was generated via MatLab’s SigLab Data Acquisition board to excite the attached PZT bimorph. Using SigLab’s VNA and VFG toolkits, a burst chirp signal with peak amplitude of 1.5 V and with frequency content ranging from 30 – 250Hz was generated to excite the PZT bimorph actuator, shown at right in Figure 6.3. The burst chirp signal was amplified by a factor of 21.5 through a Trek Amplifier (model 50/750). The velocity response of the augmented membrane was measured using the laser vibrometer at the intersections of the 5 x 4 grid shown in Figure 6.6, one point at a time. The velocity signal was fed into an Ithaco high pass filter set at 30 Hz to eliminate low frequency noise from the vacuum chamber window during operation. The filtered

signal was then sent to input Channel 2 on the SigLab DAQ board. Transfer functions were measured along the grid of the Kapton membrane. Each point was designated with a small, square piece of highly-reflective tape to help eliminate detrimental backscatter from the laser, consequently improving the quality of the measured signal.

6.4.3 Active Membrane Experimental Results

Frequency response functions relating the input excitation voltage provided to the PZT bimorphs to the measured velocity of the structure were constructed through a series of tests at vacuum conditions (10 torr) within the Tenney vacuum chamber. A sample frequency response function is plotted in Figure 6.8.

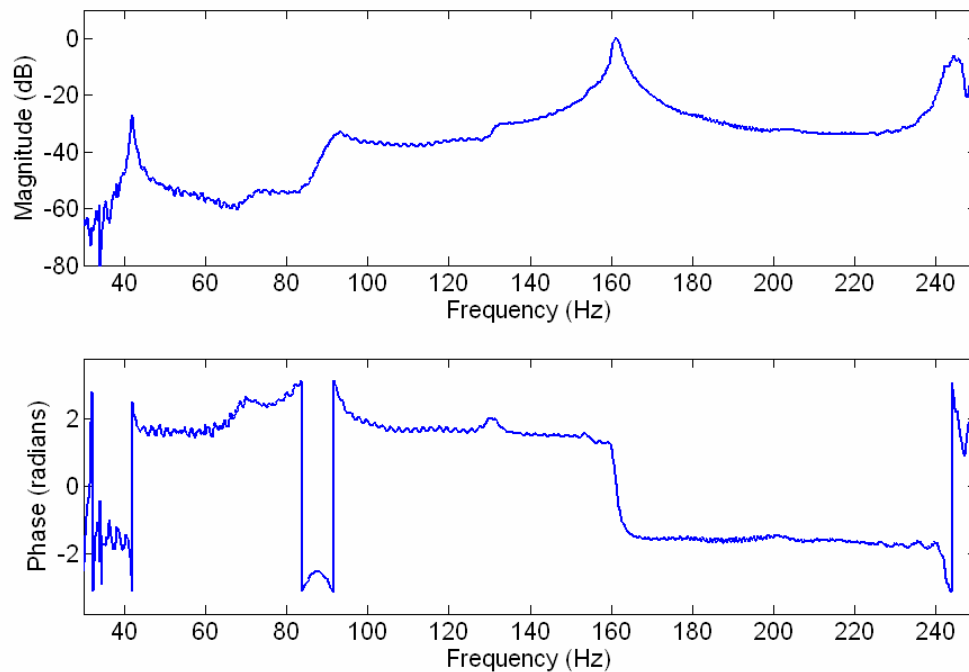


Figure 6.8. Frequency response measurement relating the input excitation voltage of the PZT bimorph to the output transverse velocity of the membrane system at 10 torr, measured (from the bottom left corner of Figure 6.6) at a point 1” along the *x*-axis and 2” along the *y*-axis.

As shown in Figure 6.8, the dominant frequencies excited in the bandwidth of 30 – 250 Hz are at 42, 94, 133, 163, and 243 Hz. Plots of the experimentally determined mode shapes of the tensioned membrane/PZT system are shown in Figure 6.10.

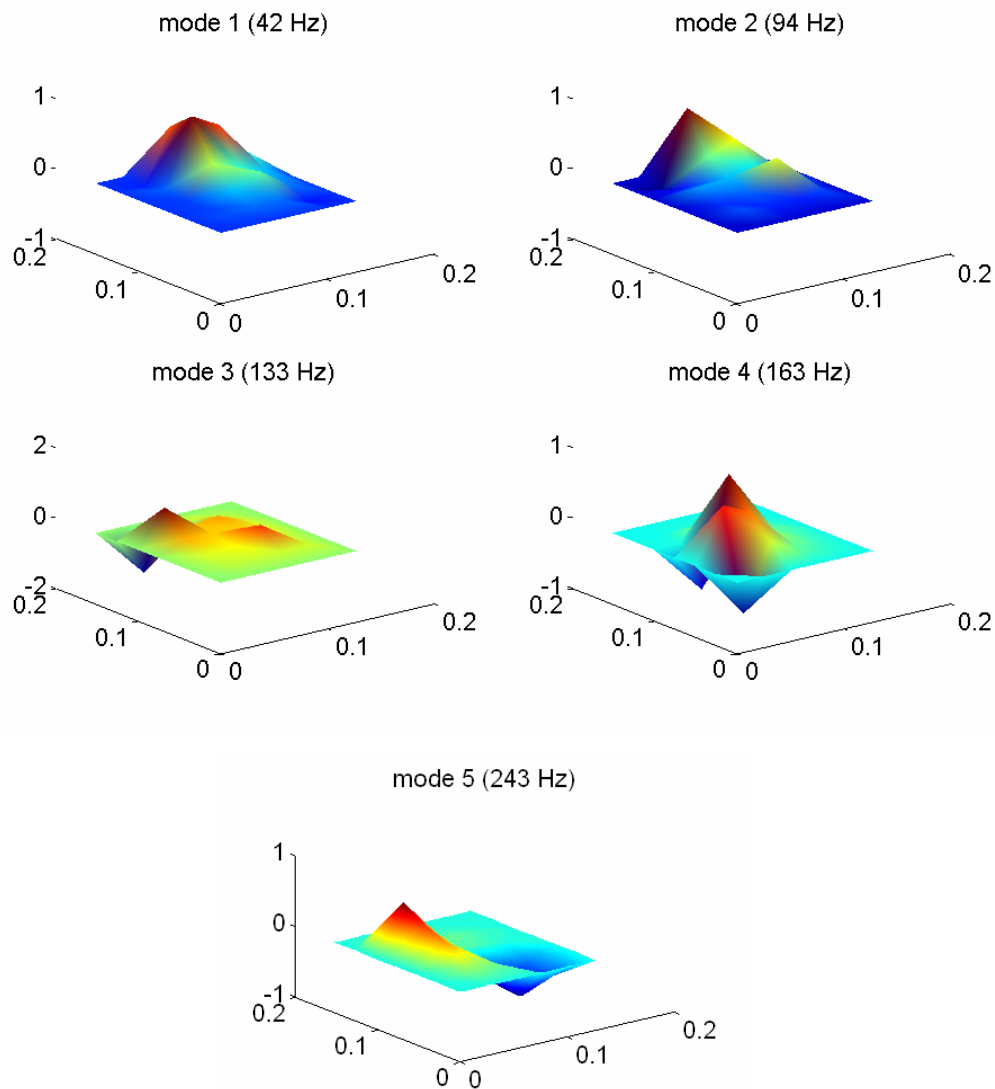


Figure 6.9. Experimentally determined mode shapes of the membrane/PZT system.

The frequencies and mode shapes identified from the experiment will now be used as a means of comparison to our finite element model.

6.4.4 Comparison between the Finite Element Model and Experimental Results

Having constructed the mass, stiffness, and damping matrices of the finite element model, the eigenvalues of the model can be computed. Solving the eigenvalue problem of the finite element model predicts the response of the system up to 250 Hz to include resonant frequencies at 43, 109, 124, 162, and 231 Hz. Plots of the associated mode shapes are shown in Figure 6.10.

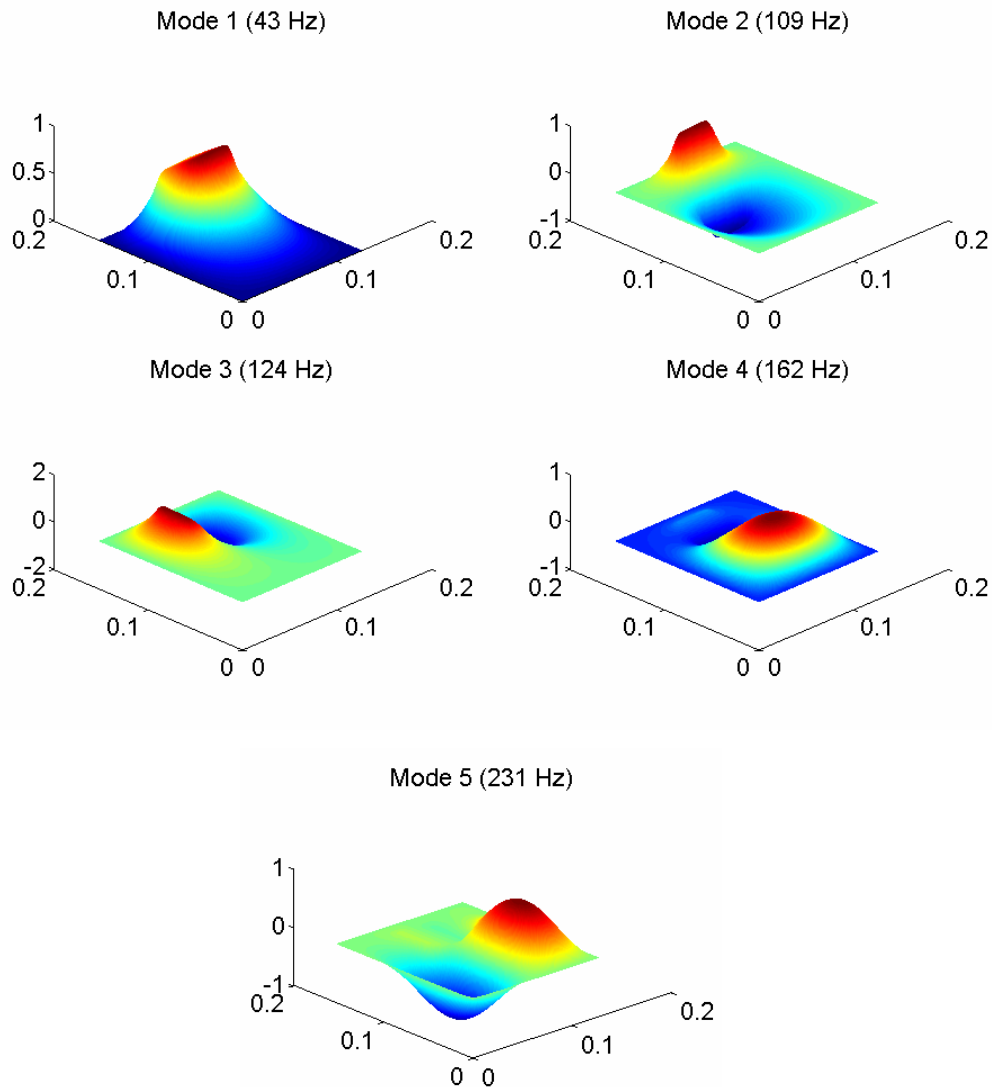


Figure 6.10. Mode shapes identified by the finite element model.

In comparing the frequencies identified by the finite element model to those identified from the dynamic analysis, good agreement is found between the model and the

experiment. A comparison between the finite element model and the experimental results is shown in Table 6.4.

Table 6.4. Comparison between the thin plate finite element model resonant frequencies and those determined via experimental analysis.

Mode #	Experiment	FEM	% Error
	Frequency (Hz)	Frequency (Hz)	
1	42	43	-2.4
2	94	109	-16.0
3	133	124	6.8
4	163	162	0.6
5	243	231	4.9

As demonstrated by Table 6.4, there is fair agreement between the model and actual experimental setup. Figure 6.11 compares the frequency response function as measured experimentally to the predicted response from the developed finite element model. The finite element model overestimates the damping present in the structure at higher frequencies.

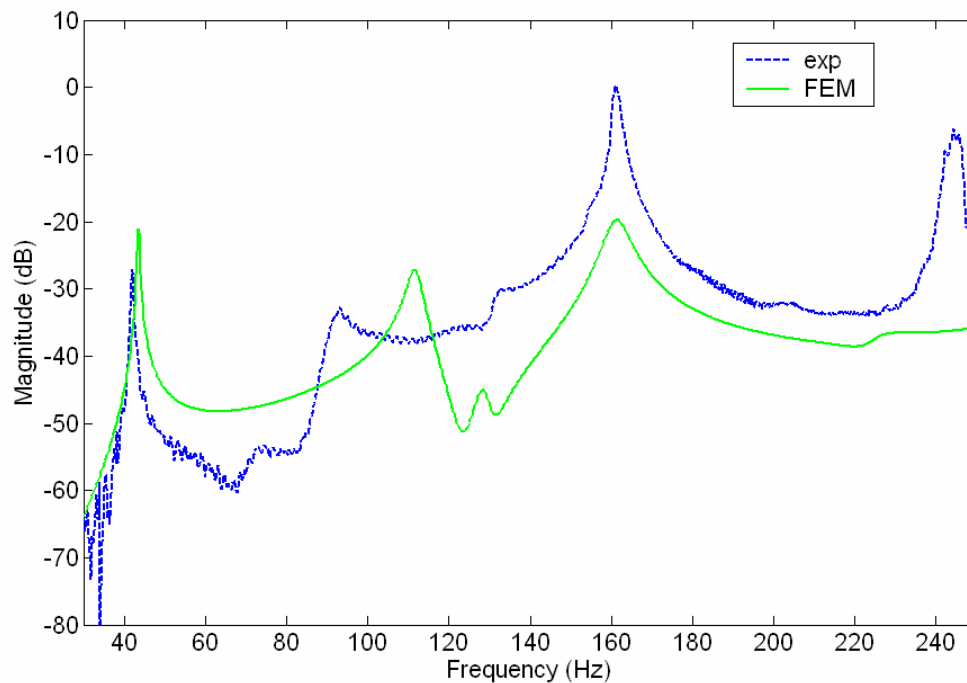


Figure 6.11. Comparison between the experimentally measured transfer function and the FEM predicted transfer function.

To reinforce the use of thin plate theory to describe the proposed augmented membrane and PZT system, a second model was developed. In this second model, only membrane theory was used, in line with the same model developed for the baseline membrane test described in Section 6.3. In contrast to the original membrane model, however, the new model considered the additional mass within the region of the added active material by allowing local changes in the density and thickness of the system. As before, the converged FE model used a grid of 20 x 24 linear elements, for a total of 480 elements. The mass per unit area within the bounded region of the PZT material was augmented to reflect the change in density as introduced by the PZT bimorph. A summary of the resultant frequencies from the finite element model is shown in Table 6.5.

Table 6.5. Comparison between experimentally determined resonant frequencies of the active membrane system and a FEM based on membrane theory and taking into account the variable density of the augmented system.

Mode #	Experiment	Membrane FEM	% Error
	Frequency (Hz)	Frequency (Hz)	
1	42	33	21.4
2	94	70	25.5
3	133	77	42.1
4	163	110	32.5
5	243	114	53.1

Although membrane theory can account for the variable mass density of the active membrane system, it cannot account for the local stiffness incurred by the additional PZT attached to the membrane since the stiffness of a membrane is a consequence of the applied tensile loading only. Consequently, membrane theory alone cannot properly account for the system dynamics, and the use of thin plate theory is validated for capturing the relevant system dynamics of the active membrane – PZT system.

6.5 Development of a 2-D LQR Controller

Now, we wish to construct an LQR controller to use the PZT bimorph as an actuator to eliminate detrimental vibration of the Kapton surface. In this section, we will first define

the LQR control problem, and then define the functional gains for this system. We will demonstrate numerically the effectiveness of the added active material when compared to the open-loop response of the pure membrane.

6.5.1 Defining the 2-D LQR Control Problem

The optimal control problem is stated as follows:

Given $z(0) \in R^{2N}$, a vector containing the states of the system, choose a control $u \in L_2(0, \infty; R^m)$ to minimize the cost functional

$$J_N(z(0), u) = \int_0^{\infty} [z(t)^T Q^N z(t) + u(t)^T R u(t)] dt. \quad (6.46)$$

Q^N is a symmetric, non-negative $2n \times 2n$ matrix, and R is a scalar value (based on the voltage supplied to each PZT of the bimorph actuator). We can define our Q^N matrix in the following manner. Following the methodology of Gibson and Adamian (1991), we will define the entries to the Q^N matrix based on the kinetic and potential energies of the system. We can thereby define

$$Q^N = \begin{bmatrix} Q_1^N & 0 \\ 0 & Q_2^N \end{bmatrix}, \quad (6.47)$$

where

$$Q_1^N = q_1 \left[\int_{\Omega} \left\{ D(\psi_i)_{xx} (\psi_j)_{xx} + D(\psi_i)_{yy} (\psi_j)_{yy} + 2D(\psi_i)_{xy} (\psi_j)_{xy} + G(\psi_i)_{xy} (\psi_j)_{xy} \dots \right\} d\Omega \right]_{i,j=1}^N + P_x(\psi_i)_{xx} (\psi_j)_{xx} + P_y(\psi_i)_{yy} (\psi_j)_{yy} \quad (6.48)$$

and

$$Q_2^N = q_2 \left[\int_{\Omega} \{ \rho h(\psi_i)(\psi_j) \} d\Omega \right]_{i,j=1}^N. \quad (6.49)$$

The terms q_1 and q_2 are weighting terms that can be determined by the control designer. For completeness, the R matrix for this particular LQR problem is defined as

$$R = r. \quad (6.50)$$

The upper and lower diagonal entries of the Q^N matrix correspond to twice the total energy of the structure (Gibson and Adamian, 2001). The optimal control, u_N , is given by

$$u_N = -K^N z(t), \quad (6.51)$$

where

$$K^N = R^{-1} [B^N]^T \Pi^N \quad (6.52)$$

and Π^N is the minimal, symmetric, non-negative solution to the Riccati equation

$$[A^N]^T \Pi^N + \Pi^N A^N - \Pi^N B^N R^{-1} [B^N]^T \Pi^N + Q^N = 0. \quad (6.53)$$

Implementing this control design with our Kapton—PZT bimorph structure, and choosing

$$[q_1 \quad q_2 \quad r] = [10 \quad 1 \times 10^6 \quad 0.01], \quad (6.54)$$

we can simulate the closed-loop response of the structure. Figures 6.12 and 6.13 show the open loop and closed-loop responses of the structure, and the required closed-loop actuation voltages, respectively.

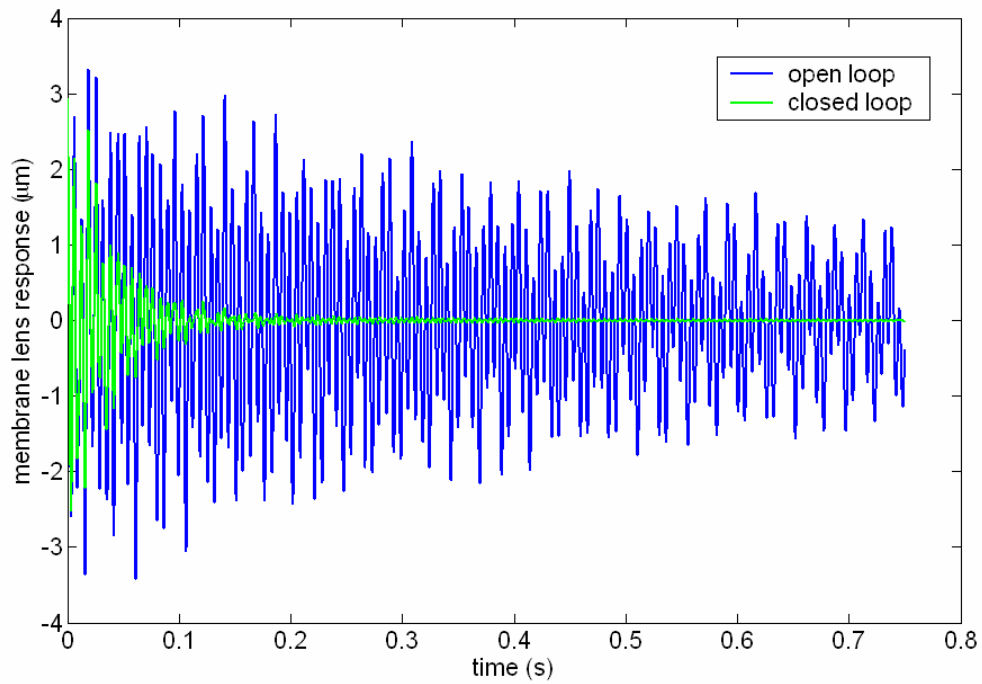


Figure 6.12 . Plot of the open (dotted) and closed (solid) loop response using the PZT bimorph actuator for structural control.

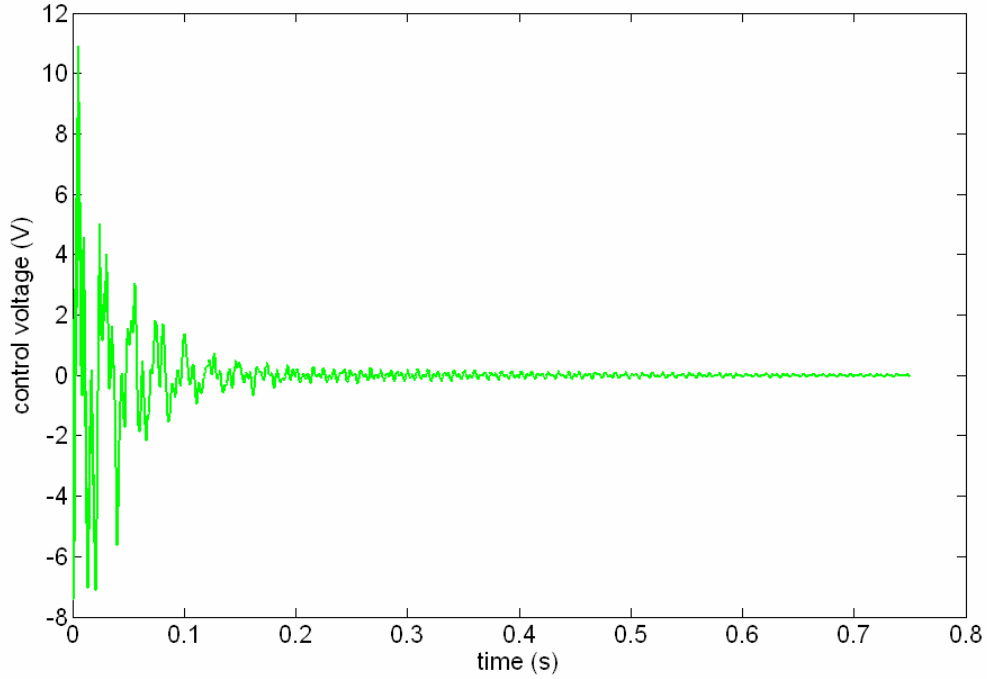


Figure 6.13. Control voltage applied to the bimorph actuator.

In comparing the closed-loop response and open loop response in Figure 6.12, we note that the control actuation induced by the PZT bimorph reduces the response of the membrane to within a micron of transverse displacement within 0.05 s using a maximum actuation voltage of 11 V.

6.5.2 Functional Gains for the Kapton Substrate System

For our active membrane system, we have already defined our Q^N and R matrices for the LQR control problem. Following the notation of Gibson and Adamian (1991), the functional gains k_s and k_v , corresponding to the strain energy and kinetic energy of our system, are the kernel functions of our approximation to the optimal control, namely

$$u^N(t) = - \langle k_s^N, z^N(t) \rangle - \langle k_v^N, \dot{z}^N(t) \rangle, \quad (6.55)$$

where, as defined previously, the notation $\langle f, g \rangle$ implies the inner product of the functions f and g . From our definition of the optimal control, $u(t)$, as stated in Equation 6.51, and combining that with Equation 6.55, we have

$$-K^N z(t) = -\begin{bmatrix} k_s^N & k_v^N \end{bmatrix} \begin{bmatrix} Q_1^N & 0 \\ 0 & Q_2^N \end{bmatrix} z(t), \quad (6.56)$$

which could also be written as

$$-K^N z(t) = -\begin{bmatrix} k_{gains}^N \end{bmatrix} [Q] z(t). \quad (6.57)$$

Since, by definition, Q is symmetric and non-negative, we can take its inverse and consequently solve for the functional gains. Doing so, we get

$$\begin{bmatrix} k_{gains}^N \end{bmatrix}^T = [Q]^{-1} [K^N]^T. \quad (6.58)$$

From our previously defined entries for the matrix Q , we can define the functional gains as

$$k_s^N = [Q_1^N]^{-1} [K^N]^T \quad (6.59)$$

and

$$k_v^N = [Q_2^N]^{-1} [K^N]^T. \quad (6.60)$$

Having defined our functional gains, we now wish to plot them for the Kapton substrate problem. When plotting, we must utilize our finite element approximation using the cubic B-splines. Therefore, we will plot the strain functional gain against the Laplacian operator acting on the global shape functions:

$$k_s = \left[(\psi_{ij})_{xx} + (\psi_{ij})_{yy} \right]_{i,j}^N [k_s^N] \quad (6.61)$$

and we plot the velocity functional gains against the global shape functions:

$$k_v = \left[\psi_{ij} \right]_{i,j}^N [k_v^N]. \quad (6.62)$$

From our defined LQR matrices, we can plot the strain and velocity functional gains of the active system. Figures 6.14 and 6.15 show the strain and velocity functional gains for the given system, respectively.

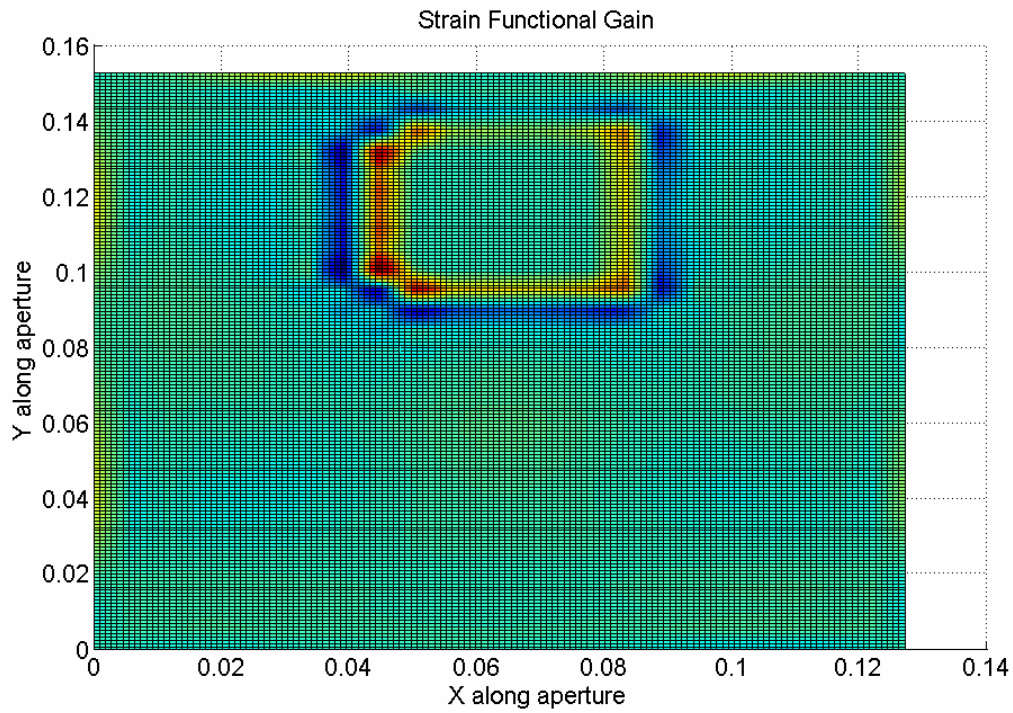
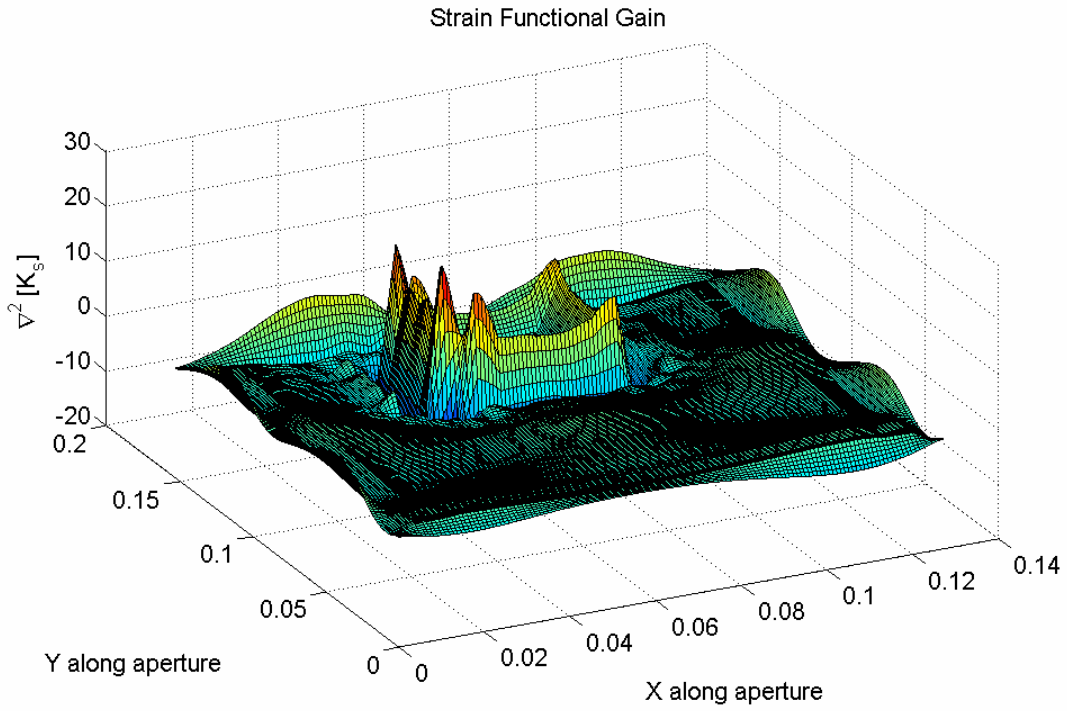


Figure 6.14. A plot of the strain functional gain within the domain of the Kapton substrate, both in an isometric (top) and top view (bottom). The finite element grid is 24 x 30, for a total of 720 elements.

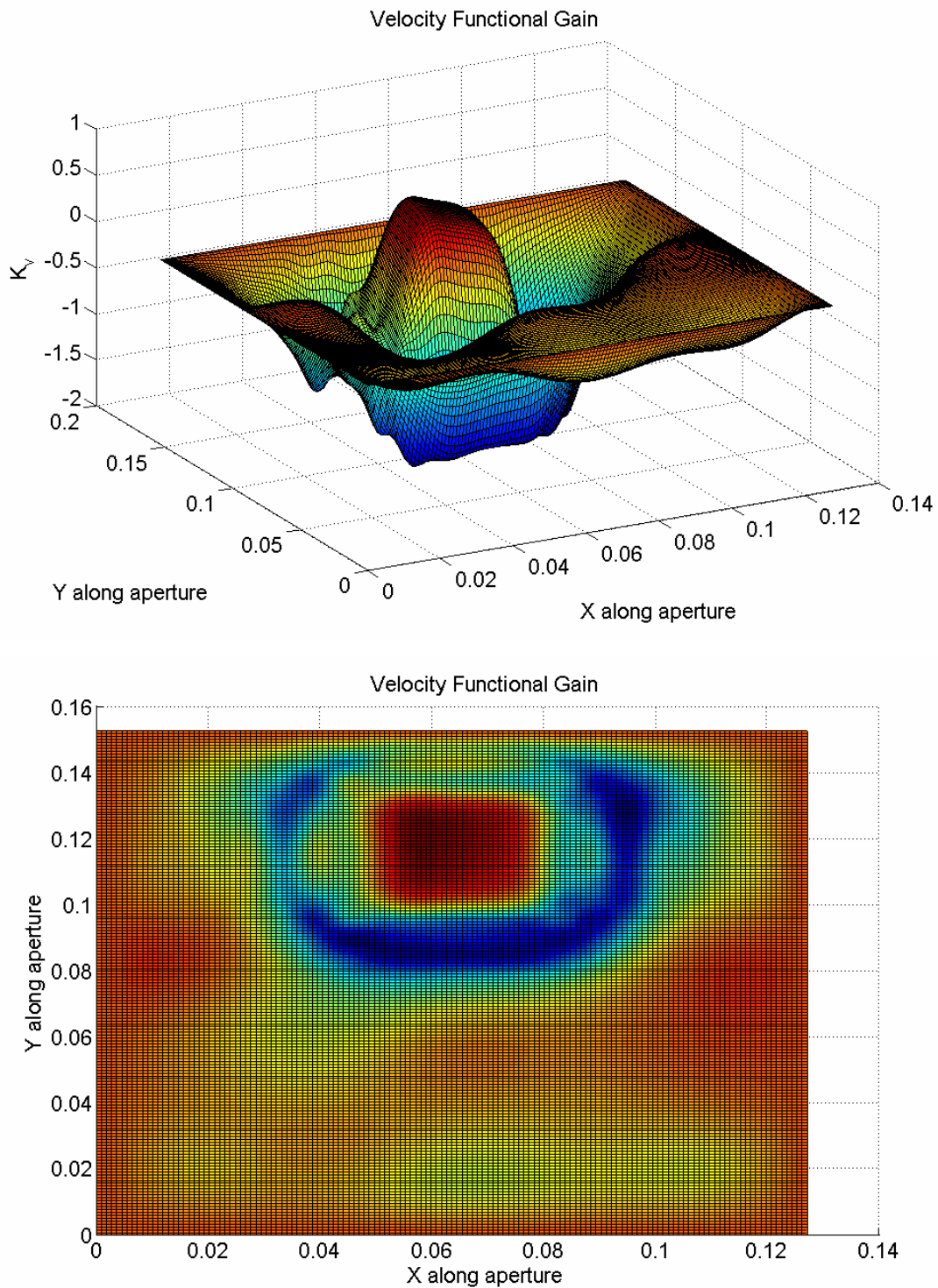


Figure 6.15. A plot of the velocity functional gain within the domain of the Kapton substrate, both in an isometric (top) and top view (bottom). The finite element grid is 24 x 30, for a total of 720 elements.

The functional gains plotted in Figures 6.14 and 6.15 reveal important information regarding the necessary sensors for effective control of the active membrane lens. In interpreting Figure 6.14, the region of vital strain sensory information is around the edges of the PZT bimorph. Strain gages placed anywhere else on the optic would be ineffective. Similarly, from a velocity standpoint, velocity measurements should be taken over the region of the PZT bimorph and around the edges of the actuator. Again, as with the strain gages, local velocity measurements taken anywhere else within the domain of the membrane lens would be ineffective.

Another important aspect of computing the functional gains is the relative magnitudes of the strain and velocity functional gains in comparison with each other. The maximum, absolute value that the strain functional gain takes is 23, while the velocity functional gain maximum, absolute value is 2. Consequently, in order to achieve control of the active membrane lens, it is more important to invest in high quality strain measurement near the edges of the PZT bimorph, as the ratio of the strain functional gain to the velocity functional gain is 11.5. In other words, there is an order of magnitude between the relative effectiveness of strain measurement as compared to velocity measurement on the structure for LQR control.

6.6 Chapter Summary

The overall goal of the present chapter was to identify the importance of using thin plate theory to capture the localized mass and stiffness effects encountered when bonding active piezoelectric material to a pre-tensioned membrane. The use of membrane theory alone cannot account for the localized stiffness changes within a composite, active membrane, and consequently fails to adequately predict the relevant dynamics of the structure.

To verify the assertion that thin plate theory must be used in designing active, augmented membrane lenses, a series of experiments were performed within a vacuum chamber. First, a pre-tensioned membrane without any augmented active material was tested within

the vacuum chamber to determine the level of pre-stress within the membrane. A developed FE model based on the use of membrane theory agreed with the first 5 identified experimental resonant frequencies to within 10% error.

Next, a set of dynamic tests were run on the same membrane structure but with a PZT bimorph augmented onto the membrane material. The PZT bimorph, 25 cm x 32 cm, was glued to the membrane and then used as the excitation actuator during a series of dynamic tests. The developed frequency response functions for the active membrane system were then compared to two models. The first FE model used thin plate theory and was able to accurately account for both the mass and stiffness effects introduced into the combined system by the introduction of a PZT bimorph onto the skin of the membrane. The results of the thin plate FE model were within 16% error on the second frequency and less than 7% for the remaining 4 frequencies.

The second model developed used membrane theory but allowed for changes in the density within the structure. From this analysis, it was determined that such a model is inaccurate for describing the dynamics of an augmented, active membrane, as the predicted frequencies were greater than 21% in error.

Next, having rigorously defined the system dynamics using thin plate theory, the LQR control problem was formulated for actively controlling the vibratory response of the membrane lens. Using numerical simulation and optimizing both the response of the membrane lens and the required control efforts of the bimorph actuator, an LQR controller was developed that could eliminate an initial disturbance within 50 ms while using a peak control effort of 11 V. As a result of this study, it can be concluded that the use of active PZT bonded to the surface of a membrane mirror or aperture could be used as a low-power, effective controller to eliminate detrimental vibration. By eliminating detrimental vibration, the membrane lens or aperture can be immediately refocused for effective imaging or telecommunication purposes.

One last study looked at the strain and velocity functional gains of the active membrane lens. From the formulated LQR control problem, both functional gains could be plotted and used for effective sensor placement within the domain of the optic. Strain information near the edges of the PZT bimorph is critical for effective control of the active membrane. Similarly, average velocity measurement should be taken over the domain of the actuator as well as around the edges of the actuator. However, where sensor cost is usually an issue, the functional gain analysis indicated an order of magnitude greater importance on collecting accurate strain information around the edges of the PZT bimorph as opposed to collecting velocity data.

Chapters 5 and 6 have focused their development on the use of active piezoelectric material to control unwanted vibrations within a membrane optic or aperture. The next two chapters will examine the effect of pressure on membrane lenses, as well as propose a novel basis from which a deformable optic could be developed.